Manuscript prepared for Biogeosciences Discuss.
with version 2014/07/29 7.12 Copernicus papers of the LaTeX class copernicus.cls.
Date: 19 July 2015

Quantifying the biological impact of surface ocean light attenuation by colored detrital matter in an ESM using a new optical parameterization

G. E. Kim, M.-A. Pradal, and A. Gnanadesikan

Department of Earth and Planetary Sciences, 301 Olin Hall, 3400 N. Charles Street, Baltimore, MD 21218, USA

Correspondence to: G. E. Kim (gracekim@jhu.edu)

Abstract

Light attenuation by colored detrital material (CDM) was included in a fully coupled Earth System Model. This study presents a modified parameterization for shortwave attenuation, which is an empirical relationship between 244 concurrent measurements of the diffuse attenuation coefficient for downwelling irradiance, chlorophyll concentration and light absorption by CDM. Two ESM model runs using this parameterization were conducted, with and without light absorption by CDM. The light absorption coefficient for CDM was prescribed as the average of annual composite MODIS Aqua satellite data from 2002 to 2013. Comparing results from the two model runs show that changes in light limitation associated with the inclusion of CDM decoupled trends between surface biomass and nutrients. Increases in surface biomass were expected to accompany greater nutrient uptake and therefore diminish surface nutrients. Instead, surface chlorophyll, biomass and nutrients increased together. These changes can be attributed to the different impact of light limitation on surface productivity versus total productivity. Chlorophyll and biomass increased near the surface but decreased at greater depths when CDM was included. The net effect over the euphotic zone was less total biomass leading to higher nutrient concentrations. Similar results were found in a regional analysis of the oceans by biome investigating the spatial variability of response to changes in light limitation using a single parameterization for the surface ocean. In coastal regions, surface chlorophyll increased by 35 % while total integrated phytoplankton biomass diminished by 18 %. The largest relative increases in modeled surface chlorophyll and biomass in the open ocean were found in the equatorial biomes, while largest decreases in depth-integrated biomass and chlorophyll were found in the subpolar and polar biomes. This mismatch of surface and subsurface trends and their regional dependence was analyzed by comparing the competing factors of diminished light availability and increased nutrient availability on phytoplankton growth in the upper 200 m. Understanding changes in biological productivity requires both surface and depth-resolved information. Surface trends may be minimal or of the opposite sign to depth-integrated amounts, depending on the vertical structure of phytoplankton abundance.

1 Introduction

The attenuation of shortwave solar radiation in the surface ocean exerts a primary control on ocean biology, since light is necessary for photosynthesis by phytoplankton. The decay of incident surface irradiance $I_{\mathrm{d}}(0,\lambda)$ with increasing depth z in the water column can be approximated as an exponential function:

$$I_{\mathrm{d}}(z,\lambda) = I_{\mathrm{d}}(0,\lambda)\exp\left(-\int_0^z k_{\mathrm{d}}(z',\lambda)\mathrm{d}z'\right), \tag{1}$$

where k_{d} (units of m^{-1}) is the spectral attenuation coefficient for downwelling irradiance. The reciprocal of k_{d} is the first e-folding depth of the incident light on the surface of the ocean, an intuitive length scale for the well-lit surface ocean. Variations in shortwave attenuation have been related to measured quantities of constituents in the aquatic medium, such as concentrations of the phytoplankton pigment chlorophyll a. Morel (1988) observed increasing k_{d} with increasing chlorophyll a pigment concentration in 176 concurrent in situ measurements, excluding stations where light attenuation was dominated by "yellow substance" or turbidity. These measurements were used to develop a function that relates k_{d} to chlorophyll a concentration of the form:

$$k_{\mathrm{d}}(\lambda) = k_{\mathrm{w}}(\lambda) + \chi(\lambda)[\mathrm{chl}]^{e(\lambda)}, \tag{2}$$

where $k_{\mathrm{w}}(\lambda)$ is the attenuation by pure seawater, [chl] is the chlorophyll a concentration and $\chi(\lambda)$ and $e(\lambda)$ are the wavelength-dependent coefficient and exponent. This parameterization implicitly includes the light attenuation of all other aquatic constituents presumed to be directly in proportion with chlorophyll concentration. Ohlmann and Siegel (2000) used a radiative transfer numerical model to develop an extended parameterization for k_{d} which depended on chlorophyll concentration, cloudiness and solar zenith angle to include the effects of varying physical conditions over ocean waters. Among these four variables, chlorophyll concentration was found to have the largest influence on reducing solar transmission below 1 m.

These initial parameterizations have been adapted for use in Ocean General Circulation Models (OGCMs) and Earth System Models (ESMs) to study the influence of spatially varying light attenuation associated with varying concentrations of phytoplankton pigments in the ocean. Although numerous model experiments of this type have been conducted, we mostly limit our introductory material to studies that utilized versions of the parameterization shown in Eq. (2). These studies examined the effects of applying a spatially varying k_{d} calculated from annual mean chlorophyll data, estimated by ocean color satellites, compared to the base case of a constant attenuation depth. Murtugudde et al. (2002) employed the Morel parameterization (Eq. 2) spectrally averaged over visible wavelengths, from 400 to 700 nm, to calculate $k_{\mathrm{d}}(\mathrm{vis})$ using chlorophyll a concentration estimates from the Coastal Zone Color Scanner (CZCS). Spatially varying the attenuation depth improved the OGCM SST simulation in the Pacific cold tongue and during ENSO events and in the Atlantic near river outflows. Subsequent studies employed an optics model that separately attenuated visible light in two bands of equal energy, nominally the "blue-green", $k_{\mathrm{d}}(\mathrm{bg})$, and "red" bands, $k_{\mathrm{d}}(r)$, as specified in (Manizza et al., 2005):

$$k_{\mathrm{d}}(\mathrm{bg}) = 0.0232 + 0.074 \cdot [\mathrm{chl}]^{0.674} \tag{3}$$

$$k_{\mathrm{d}}(r) = 0.225 + 0.037 \cdot [\mathrm{chl}]^{0.629}. \tag{4}$$

Studies that applied this k_{d} parameterization in ESMs were uniquely able to assess how changes in oceanic shortwave absorption can affect atmospheric and oceanic circulation via changes in sea surface temperature (SST). Gnanadesikan and Anderson (2009) observed changes in strength of the Hadley and Walker circulations when applying a spatially-varying k_{d} using chlorophyll concentration from the SeaWiFS (Sea-viewing Wide Field-of-view Sensor) ocean color satellite relative to a clear ocean with no chlorophyll. Alternatively, Manizza et al. (2005) applied this parameterization to an OGCM with a biogeochemical model to calculate k_{d} using modeled chlorophyll concentration instead of surface chlorophyll estimates from satellite. The main advantage of the latter model configuration is that phytoplankton can respond to changes in environmental variables. They found that adding phytoplankton amplified the seasonal cycles of SST, mixed layer depth and sea-ice cover,

which in turn created environmental conditions that were favorable to additional phytoplankton growth.

Variations in light attenuation in ESMs were previously attributed to chlorophyll and implicitly to aquatic constituents assumed to vary in proportion to chlorophyll. Other optically significant aquatic constituents can now be explicitly incorporated into models. This paper is concerned with the omission of colored detrital material (CDM) in approximations of light decay in the current generation of ESMs. CDM consists of chromophoric dissolved organic matter (CDOM) and non-algal detrital particles (NAP). It is operationally defined by its spectrally-dependent absorption coefficient of light, a_{dg} (units of m^{-1}), which represents the fraction of incident power that is absorbed by detrital matter in a water sample over a given pathlength. The absorption coefficient is given the subscript "dg" to represent the sum of the two component absorption coefficients; (1) non-algal detrital particles, a_{NAP}, and (2) light-absorbing dissolved organic matter which passes through a 0.2–0.4 µm filter, a_{CDOM}, (called *gelbstoff* by early researchers in optical oceanography, hence the "g" in "dg"): $a_{\mathrm{dg}} = a_{\mathrm{NAP}} + a_{\mathrm{CDOM}}$. Measurements suggest CDOM accounts for a large fraction of non-water absorption in the open ocean in the UV and blue wavelengths (Siegel et al., 2005; Nelson and Siegel, 2013). The attenuation of light by this strongly absorbing component should be included in Earth System Models. Although light absorption by NAP is a small fraction of CDM absorption (see Fig. 1), the sum of NAP and CDOM is considered because existing satellite algorithms cannot separate the contribution of each component.

Parameterizing k_{d} using Eq. (2) relies on the validity of the bio-optical assumption, which states that all light-attenuating constituents covary with chlorophyll concentration. Yet processes that influence CDM abundance, such as freshwater delivery of terrestrial organic matter and photobleaching, can behave independently of chlorophyll a concentration, rendering the bio-optical assumption inappropriate for some aquatic environments. In an analysis of satellite ocean color data products, Siegel et al. (2005) show correlation between chlorophyll and CDM distributions in subtropical gyres and upwelling regions. These variables are found to be independent in subarctic gyres, the Southern Ocean and coastal regions influenced by land processes such as coastal and river runoff. In this paper, we will

consider the impact of decoupling the optical influence of chlorophyll a and CDM in Earth System Models.

Recent studies have incorporated the optical properties of additional in-water constituents into global ocean biogeochemical simulations. Gregg and Casey (2007) calculate in-water radiative properties using the absorption and scattering of water, phytoplankton groups and CDOM in a coupled ocean circulation-biogeochemical-radiative model. Dutkiewicz et al. (2015) assess the bio-optical feedbacks of detrital matter, CDOM and phytoplankton by explicitly representing these components in their ocean biogeochemistry-ecosystem model. In this paper we use a fully coupled Earth System Model to better understand how changes in light attenuation from including CDM affect ocean ecosystems.

In Sect. 2, we introduce the global ocean color dataset for the absorption coefficient of detritus and CDOM, and discuss its incorporation into the GFDL CM2Mc ESM with BLING biogeochemistry model. This is accomplished using a newly developed parameterization for $k_{\mathrm{d}}(\lambda)$, which aims to represent light attenuation by chlorophyll a and CDM as independently varying phenomena. (For the remainder of this paper, we will refer to chlorophyll a concentration simply as chlorophyll.) Section 3 details the model runs and the results, with a focus on how changes in light affect chlorophyll, biomass and nutrient concentrations. The paper concludes with Sect. 4, discussing the implications of our findings and suggestions for future work.

2 Methodology

2.1 Light penetration parameterization

A new k_{d} parameterization was developed for implementation in the GFDL CM2Mc ESM (Galbraith et al., 2011) with BLING ocean biogeochemistry (Galbraith et al., 2010). In its current configuration, the CM2Mc-BLING system uses the Manizza et al. (2005) optics model and k_{d} parameterization as shown in Eqs. (3) and (4). The new parameterization was developed from this optics model, revising the $k_{\mathrm{d}}(\mathrm{bg})$ parameterization only (Eq. 3).

The $k_d(r)$ parameterization was unchanged because light absorption by CDOM is very small compared to absorption by seawater and chlorophyll in the red wavelengths. This is apparent by examination of the spectral shapes of these constituents in Fig. 1. The new $k_d(\mathrm{bg})$ parameterization incorporates the absorption coefficient of detritus and CDOM at wavelength 443 nm, $a_{dg}(443)$, because existing satellite data products of a_{dg} are readily available for this wavelength only.

In the new parameterization, the dependence of $k_d(\mathrm{bg})$ on both chlorophyll concentration and $a_{dg}(443)$ is the best fit function between concurrent in situ measurements of these variables from the NASA bio-Optical Marine Algorithm Dataset (NOMAD) (Werdell and Bailey, 2005). Measurements of k_d from 400 to 530 nm were energy-weighted and averaged to get a single value for the attenuation coefficient in the blue-green wavelengths. There were 244 concurrent measurements of $k_d(\mathrm{bg})$, chlorophyll concentration and $a_{dg}(443)$ from the NOMAD dataset, representing both coastal and open ocean waters. The locations of these measurements are shown in Fig. 2. The stations were arbitrarily grouped by region and color coded: (1) western Atlantic, northern cluster in black; (2) western Atlantic, Amazon river outflow and offshore stations in green; (3) Antarctic peninsula in orange; (4) Southern Ocean in blue; (5) western Pacific in magenta; (6) stations across the Pacific ocean in red and (7) eastern Pacific in cyan. We found poor correlation between chlorophyll concentration and $a_{dg}(443)$ at these stations, as shown in Fig. 3. The best fit surface for $k_d(\mathrm{bg})$, chlorophyll concentration and $a_{dg}(443)$ was found using a least-squares polynomial regression model using the Levenberg-Marquardt algorithm, resulting in the following parameterization:

$$k_d(\mathrm{bg}) = 0.0232 + 0.0513 \cdot [\mathrm{chl}]^{0.668} + 0.710 \cdot a_{dg}(443)^{1.13}. \quad (5)$$

We conducted a sensitivity analysis to assess the importance of each region for obtaining the parameters by removing one regional cluster from the regression fitting at a time. The parameters were mostly stable. The exponent to the chlorophyll term was the only term that changed by an amount that well exceeded the fitting uncertainty, increasing by 0.23 when the eastern Pacific stations were omitted.

Figure 4 panels (a) and (b) show an improved fit between modeled and measured $k_{\mathrm{d}}(\mathrm{bg})$ when using Eq. (5). Equation (5) is qualitatively different from the previous parameterization, Eq. (3), in several ways. The attenuation coefficient is less dependent on chlorophyll concentration, with a smaller coefficient and exponent on the chlorophyll term in Eq. (5) compared to Eq. (3). Meanwhile, the additional $a_{\mathrm{dg}}(443)$ term makes the water more opaque in locations where CDM and chlorophyll concentration are not well correlated, such as coastal zones that are strongly influenced by the terrestrial delivery of CDOM. The k_{d} dependence on $a_{\mathrm{dg}}(443)$ is superlinear, which at first glance seems to suggest an unexpectedly strong dependence on CDOM and detrital particles. We suggest this superlinear relationship is justified because the parameterization is fitting for spatial variations in CDOM quality and quantity. Measurements of a_{dg} across the ultraviolet to visible spectrum suggest the spectral dependence of light absorption by CDOM is regionally specific (Nelson and Siegel, 2013).

2.2 Implementation in ESM

This parameterization was implemented in the GFDL CM2Mc ESM, a coarse resolution coupled global climate model with land, ice, atmosphere and ocean components (Galbraith et al., 2011). The Modular Ocean Model version 4p1 code is used to simulate the ocean. The model has a varying horizontal resolution from 1.01 to 3.39° and 28 vertical levels of increasing thickness with depth. Ocean biogeochemistry is represented by the Biogeochemistry with Light, Iron, Nutrients and Gases model (BLING), which is embedded in the ocean component of the physical model (Galbraith et al., 2010). The coupling between the biogeochemical model and physical model allows changes in chlorophyll concentration to produce changes in shortwave radiation absorption and vice versa. Since the same optical model is used for calculating light attenuation for physics and biology in our ESM configuration, the same attenuation depth is used in simulating physical processes and biological productivity. For example, the optical model calculates light attenuation using model-derived chlorophyll concentration. Increases in chlorophyll concentration reduce the attenuation depth, reducing total light available for biological processes such as photosynthesis and physical processes such as the total shortwave heating of the ocean. However, by utilizing one op-

tical parameterization for the entire ocean, regionally-specific variations of the functional dependence of light attenuation on chlorophyll and CDM are not represented in this model setup.

In the BLING biogeochemical model, phytoplankton growth rate is calculated implicitly as a function of temperature, macronutrient concentration, iron concentration and light.

$$\mu = P_0^{\mathsf{C}} \times \exp(kT) \times \mathrm{nlim} \times \mathrm{llim} \tag{6}$$

where μ is a carbon-specific growth rate, P_0^{C} is a maximum growth rate at 0 °C, $\exp(kT)$ is a temperature-dependent term based on Eppley (1972), $\mathrm{nlim} = \min(\mathrm{Fe_D}, \frac{\mathrm{PO_4}}{k_{\mathrm{PO_4}}+\mathrm{PO_4}})$ is a nutrient limitation term following a Liebig's law of the minimum and $\mathrm{llim} = (1 - \exp(\frac{-I}{I_k}))$ is a light limitation term. These nutrient and light limitation factors, nlim and llim, represent the extent to which the optimal photosynthetic growth rate is scaled down by nutrient and light availability. Mathematically, nlim and llim have values between 0 and 1 that scale down the optimal photosynthetic rate as they are multiplied by P_0^{C}. Furthermore, these are the only two variables that determine biomass in the BLING model. Total biomass is a sum of large and small phytoplankton groups, which are related to growth rate μ by the following equation

$$B = B_{\mathrm{large}} + B_{\mathrm{small}} = P^* \left(\left(\frac{\mu}{\lambda}\right)^3 + \left(\frac{\mu}{\lambda}\right) \right) \tag{7}$$

where B is biomass, P^* is a scale factor for phytoplankton concentration and λ is a temperature-dependent mortality rate

$$\lambda = \lambda_0 \times \exp(kT). \tag{8}$$

Substituting Eqs. (6) and (8) for μ and λ into Eq. (7), gives us

$$B = P^* \left(\left(\frac{P_0^{\mathsf{C}} \times \exp(kT) \times \mathrm{nlim} \times \mathrm{llim}}{\lambda_0 \times \exp(kT)} \right)^3 + \left(\frac{P_0^{\mathsf{C}} \times \exp(kT) \times \mathrm{nlim} \times \mathrm{llim}}{\lambda_0 \times \exp(kT)} \right) \right) \tag{9}$$

Following Dunne et al. (2005), the temperature dependence of the mortality rate is set identical to that of the growth rate such that the $\exp(kT)$ term in both μ and λ expressions are identical, Eq. (9) reduces to the following relationship between biomass, nutrient limitation and light limitation

$$B \propto (C(\text{nlim} \times \text{llim})^3 + (\text{nlim} \times \text{llim})). \tag{10}$$

where C is a constant. Dunne et al. (2005) found that such a formulation was able to reproduce the observed phytoplankton size structure across 40 sites. This allows us to separately evaluate the contributions of nutrient and light limitation to changes in biomass in our biogeochemical model. This relationship will be utilized in the Results section of our paper.

Chlorophyll concentration is calculated from biomass using a varying chl : C ratio to account for photoadaptation. Large scale patterns and features of chlorophyll concentration are qualitatively represented, with lower chlorophyll concentration in the gyres and higher concentrations in mid- to high-northern latitudes and equatorial upwelling zones (see Fig. 5). In general, the annual average modeled chlorophyll exceeds the satellite observed chlorophyll concentration in the open ocean. The seasonal cycle is also well-represented, but with a northern latitude spring bloom onset earlier than appears in satellite data. There is good spatial agreement between the modeled and observed spatial distribution of macronutrients, which is shown in Fig. 6. BLING only models phosphate concentration, which is comparable to an "average macronutrient" that represents the average concentrations of phosphate and nitrate scaled to phosphate by the N : P Redfield ratio, $\frac{1}{2}(PO_4 + \frac{NO_3}{16})$ (Galbraith et al., 2010). The error in chlorophyll and nutrient concentrations in this implementation of BLING are worse than in Galbraith et al. (2010) because the model parameters were originally tuned to a data-driven ocean model. As a result, errors that appear in the physical circulation will also appear in the biological solution.

The ocean optical model receives incoming shortwave radiation from the atmospheric component. Visible light is divided and then averaged into two spectral bands, blue-green and red, which are then attenuated by $k_d(\text{bg})$ and $k_d(r)$ respectively. In its previous configuration, BLING calculated $k_d(\text{bg})$ as a function of chlorophyll concentration as shown in

Eq. (3). For this study, k_d(bg) is calculated using Eq. (5) with model-predicted chlorophyll concentration and fixed $a_{dg}(443)$ from satellite climatology. The $a_{dg}(443)$ dataset used in this study is the average of the 2002 to 2013 Aqua MODIS GSM $a_{dg}(443)$ Level 3 annual composites from http://oceancolor.gsfc.nasa.gov. Annual average data was used instead of monthly data to maximize the number of grid cells with unimpeded satellite observations. Consequently the seasonal variability of CDM is not represented in our model runs. By fixing $a_{dg}(443)$ as a constant value throughout the year, light absorption by CDM is underestimated in months where riverine and coastal runoff deliver additional CDOM to the ocean. The averaged satellite data was re-gridded to the ocean model's spatial resolution and missing values were filled in by equal weight averaging over the pixel's 8 neighbors using Ferret, a data visualization and analysis tool for gridded datasets (see Fig. 7). Satellite-estimated values of surface $a_{dg}(443)$ were held constant with increasing depth.

3 Model runs: setup, results and discussion

3.1 Model setup

The GFDL CM2Mc ESM with BLING ocean biogeochemistry was spun up for 1500 years with the Manizza et al. (2005) ocean optics model, allowing dynamical processes to reach equilibrium. New model runs were initialized from this spun up state and were completed for an additional 300 years. We analyzed the final 100 years of the model runs to average over interannual variability and to eliminate the influence from spinup, which we consider to be the period of time it takes for a distinct signal to develop. For the model experiments discussed in this paper the spinup time was less than 50 years. The data presented in this section are average results from the final 100 years of the two model runs: the (1) "chl&CDM" run utilizes the full k_d(bg) parameterization, Eq. (5), while the (2) "chl-only" run calculates light attenuation with the chlorophyll-dependent term only: $k_d(\text{bg}) = 0.0232 + 0.0513 \cdot [\text{chl}]^{0.668}$. The difference between the two model runs (chl&CDM minus chl-only) shows the impact

of added shortwave attenuation by CDM. For the remainder of this paper we will refer to k_{d}(bg) as k_{d} for simplicity.

The SST contour plot in Fig. 8a shows modeled (chl&CDM) minus observed using NOAA_OI_SST_V2 data provided by the NOAA/OAR/ESRL PSD, Boulder, Colorado, USA, from their web site at http://www.esrl.noaa.gov/psd/ (Reynolds, 2002). The RMS error between annually averaged modeled and observed SST is 1.5°C. Additional validation details for the physical ocean model can be found in Galbraith et al. (2011). The chl-only model run minus observed is not shown because the differences are qualitatively similar to those shown in Fig. 8a. The differences in SST between the chl&CDM and chl-only model runs (in Fig. 8b) are generally small in the annual mean and do not cause a significant change in the RMS error.

3.2 Model results: global trends

Adding CDM to the k_{d} parameterization shoaled the attenuation depth (k_{d}^{-1}, in m) in most places. This change in the light field was accompanied by a globally integrated 10 % increase in surface macronutrients, 11 % increase in surface biomass and 16 % increase in surface chlorophyll. These changes reflect the total value from the surface grid boxes, which represent the uppermost 10 m. At first glance, this result was puzzling since increases in chlorophyll and biomass are generally associated with increased nutrient consumption, which is usually indicated by decreased nutrient concentration. Instead, all three variables increased together. The spatial distributions of surface changes in macronutrients, chlorophyll concentration and biomass are shown in Fig. 9.

In order to understand these surface changes, it is necessary to evaluate changes in the biomass depth profile. Globally averaged biomass and particulate organic carbon (POC) export flux in the chl&CDM run are higher near the surface but diminished at depth, as shown in Fig. 10. Chlorophyll increases at the surface, but below 25 m there is less biological productivity in the chl&CDM run. The depth-integrated result is a 9 % decrease in total biomass. Furthermore, since biological productivity is occurring closer to the surface, particulate matter is remineralized in the water column and less is exported into the deep

ocean. This can be seen in Fig. 10b. The cumulative effect is a 7 % decrease in POC flux at 200 m.

This upward shift in the vertical distribution of biomass was accompanied by increased macronutrients at all depths. Here, we will consider the distribution of macronutrients in the top 200 m as a measure of the biological activity in the mixed layer according to the biological pump efficiency, E_{bp}, defined in Sarmiento and Gruber (2006) as: $E_{\mathrm{bp}} = \frac{C_{\mathrm{deep}} - C_{\mathrm{surface}}}{C_{\mathrm{deep}}}$. This metric provides a indication of the extent to which phytoplankton are able to draw down nutrients delivered to the surface from the deep ocean. Here, C_{surface} is the integrated nutrient concentration between 0 and 100 m and C_{deep} is the integrated nutrient concentration between 100 and 200 m. The difference in E_{bp} between the two model runs shows a widespread decrease in biological pump efficiency when CDM is included (see Fig. 11). In a global average sense, increased light limitation by CDM diminishes total biomass, leaving excess nutrients in the water column. Nutrients are more abundant and phytoplankton are less effective at utilizing them when the ocean is more light limited. The spatial correlation between the difference in E_{bp} and a_{dg} is -0.26, indicating a general negative relationship between the two variables. However, regions of greatest light absorption by CDM are not always the same regions of greatest decrease in E_{bp} for reasons that will be discussed in the following subsections.

3.3 Ocean biomes

The analysis in this section will address changes in nutrient concentration and biological productivity by ocean biome. Following Sarmiento et al. (2004), we use average vertical velocity, maximum wintertime mixed layer depth and sea ice cover to define six biomes that are differentiated based on physical circulation features. They are: (1) equatorially influenced, between 5° S and 5° N, divided into upwelling and downwelling regions, (2) marginal sea ice zones that are covered by sea ice at least once during the year, (3) permanently stratified subtropical biomes where downwelling occurs and maximum mixed layer depth is ≤ 150 m, (4) seasonally stratified subtropical biomes where downwelling occurs and maximum mixed layer depth >150 m, (5) low-latitude upwelling regions between 35° S and 30° N, and (6) all

subpolar upwelling regions north of 30° N and south of 25° S. Boundaries were determined based on circulation features from the respective model runs for consistency. See Fig. 12 for a visual representation of biome extent for the chl&CDM model run.

The largest changes in biome areal extent include a 19 % increase in the Northern Hemisphere marginal ice zone and −9 % change in the extent of the neighboring subpolar Northern Hemisphere biome, as shown in table 1. The biome area changes between the two model runs because the biological and physical models are coupled. The added light attenuation by CDM in the optical model affects both biological production and physical variables such as SST in our ESM configuration. Furthermore, the changes in chlorophyll concentration from the increased light attenuation change the attenuation depth in the physical model.

Differences in surface chlorophyll, biomass and macronutrients between the two model runs (see table 2) show that the addition of CDM results in several important qualitative and regionally specific changes. For example, the greatest relative change in chlorophyll and biomass over the upper 10 m are found in equatorial and low latitude biomes, with 15–17 % increases in biomass and 21–24 % increases in chlorophyll. Meanwhile, the greatest changes in depth-integrated chlorophyll and biomass are found in high latitude regions. In the Northern Hemisphere subpolar biome, chlorophyll decreased by 14 % and biomass decreased by 15 %. Chlorophyll and biomass decreased by 9 and 10 % respectively in the Southern Hemisphere marginal ice zone. The following analysis seeks to understand this mismatch between surface and subsurface trends between biomes. In particular, why are the largest changes in surface chlorophyll near the equator and largest changes in depth-integrated chlorophyll at higher latitudes?

As shown in previous sections, phytoplankton increase at the surface and decrease below when CDM is included. The resulting vertical profile of chlorophyll is altered in different ways depending on the biome. To illustrate, we choose three representative biomes from various latitudes, for which chlorophyll profiles are shown in Fig. 13. In the equatorial upwelling and seasonally stratified biomes, the deep chlorophyll maximum is increased. In the ice NH region, where light delivery is seasonally dependent, chlorophyll is found in highest

concentrations near the surface and is diminished at depth. In every biome, there is more chlorophyll near the surface but less chlorophyll beyond some depth. These changes can be attributed to a combination of diminished light availability and increased nutrient availability.

Over the upper 200 m, there are more nutrients and less irradiance at all depths. Referring back to Fig. 10a, there is more biomass near the surface, but diminished biomass at depth. These plots show that as we move down the water column, there is a changing balance of nutrient and light availability affecting phytoplankton growth. The increased abundance of nutrients fuels the growth of phytoplankton near the surface. At depth, light limitation is increased to a level that results in diminished phytoplankton productivity.

We analyze the competition of light and nutrient availability on biomass using the light and nutrient limitation factors previously discussed in the Methodology section. The average light and nutrient limitation scaling factors over the surface 10 m of each open ocean biome and the coastal region for the chl-only run are shown in Fig. 14a. The coastal region was defined as grid cells adjacent to land. Consider the placement of the various biomes on this plot for the model run where light attenuation depends on chlorophyll alone. The equatorial regions are least light limited, so they lie to the right on the x axis. The marginal ice zones and subpolar regions are most light limited and lie to the left on the x axis. The Southern Hemisphere biomes are in general more nutrient limited than their Northern Hemisphere counterparts, due to modeled iron limitation. They are found lower on the y axis.

As additional light limitation is introduced by the inclusion of light absorption by CDM in the k_{d} parameterization, these markers shift. Panel b of Fig. 14 shows nlim and llim averaged over the surface 10 m for the chl&CDM model run. The displacement of each point from panel a to its new coordinates in panel b are shown in vector form in panel c. The vector begins at its coordinates from panel a, i.e. values from the chl-only run, and terminates with an "x" at the new coordinates from the chl&CDM model run. This vector indicates the change in nutrient and light limitation between the two model experiments.

The impact of these changes in light and nutrients on biomass can be seen by overlaying lines of constant biomass on these plots. Using Eq. (10), we utilize the fact that in the BLING model, biomass scales as $(C(\mathrm{nlim} \times \mathrm{llim})^3 + (\mathrm{nlim} \times \mathrm{llim}))$. In panel c, all biome vectors are

pointed in the left and upward direction, indicating more nutrient availability and less light availability. The vectors cross contours of constant biomass in the direction of increasing biomass. Additional nutrient availability fuels increases in biomass in the upper 10 m of the ocean in almost every ocean biome, which is in agreement with the results reported in table 2. Panel d is similar to panel c, but with nlim, llim values averaged over the upper 200 m of the ocean. Here, the vectors are moving in a direction that crosses lines of decreasing biomass. This is consistent with results shown in table 3. In this case, the decrease in light availability drives the decrease in biomass, despite the increase in nutrients.

The two clusters of vectors, i.e. nlim and llim averaged over (1) 0 to 10 m constituting a "euphotic regime" and (2) 0 to 200 m constituting a "subsurface regime", are shown on the same plot for comparison in Fig. 15. To first order, we think of the euphotic regime as the depth range that dominates the signal seen by satellite observations and the subsurface regime as the integrated impact over the entire ecosystem. The key difference between the two regimes is the vectors in the surface regime are crossing lines of constant biomass in the increasing biomass direction, while the vectors in the subsurface regime are crossing lines of constant biomass in the decreasing biomass direction. While there is a noticeable difference in the magnitude and angle of the vectors between these two regimes, these differences are only meaningful in the context of the vector's placement in the domain. For example, the greatest decreases in depth-integrated biomass from the inclusion of CDM were found in high latitude biomes and coastal region. This is most pronounced in the coastal region, where biomass diminished by 18 %. The corresponding magenta vector in this plot noticeably spans the greatest distance in the direction of decreasing biomass contour lines. Although the vector for the Northern Hemisphere marginal ice zone ("ice nh") is smaller, it is placed in the upper left hand corner where the contour lines are closer together. It crosses the appropriate number of lines of constant biomass to produce the 10 % drop in biomass in this region when CDM is included. In the surface regime, the greatest increases in biomass are in the equatorial biomes. While the "eq up" and "eq down" vectors are short, shown in Fig. 14c, the slope of the vector results in sufficient positive displacement in the y direction to produce increasing biomass. The slope of some

of the higher latitude vectors, such as the seasonal stratified biomes are more parallel to the lines of constant biomass, which accounts for the smaller changes in surface biomass.

Increases in surface chlorophyll ranged from 15 to 24 % in the equatorial, low-latitude and permanently stratified biomes. In these areas, depth-integrated biomass decreased by ≤ 6 %. These biomes comprise the cluster of vectors on the bottom right hand side of the plot in Fig. 15. The variation in surface chlorophyll appears to depend on the seasonal availability of light, since the biomes are similarly nutrient limited. In these biomes, shoaling the euphotic zone concentrates phytoplankton closer to the surface. In equatorial and low-latitude regions, the steady supply of light and upwelling currents keep phytoplankton near the surface mostly year-round. Here, surface chlorophyll increased by 21 to 24 %. In the permanently stratified biome, there are intermittent mixing events and, on average, downwelling currents. Mixing the phytoplankton throughout the water column has the effect of reducing the concentration of phytoplankton near the surface. Any increases in surface chlorophyll in the stratified regions will be intermittent and when annually averaged smaller than the changes found near the equator, which explains why surface chlorophyll increased by 15 % in the permanently stratified biome.

3.4 Coastal regions and model error

The spatial distribution of light absorption by CDM in Fig. 7 and diminished attenuation depth in Fig. 9 suggest the addition of CDM to the optical model would have a significant impact on ocean productivity in coastal regions. For the following analysis, the coastal region was defined as grid cells adjacent to land.

In coastal regions, surface nutrients increased by 16 %, surface biomass by 22 % and surface chlorophyll by 35 %. Depth-integrated trends were of the opposite sign compared to surface trends. Total biomass decreased by 18 % and total chlorophyll decreased by 17 % when CDM was included. The largest percentage change in integrated biomass was found in the equatorial latitudes, where there was up to a 38 % drop in coastal biomass. High northern latitudes north of 60° N experienced 17–36 % decreases in coastal biomass. These results are reported with the understanding that the coastal circulation is likely to

be poorly resolved in our coarse model. Nonetheless, they highlight the potential impact of including the optical impact of CDM in coastal regions.

The results shown in this paper compare the "chl&CDM" and "chl-only" model runs. A comparison of the output of the "chl&CDM" model run and a model run with the original k_{d} parameterization, Eq. (3), show qualitatively similar trends in coastal regions. Surface nutrients increased by 1 %, surface biomass by 3 % and surface chlorophyll by 6 %, while depth-integrated biomass and chlorophyll decreased by 9 % ("chl&CDM" minus model run using Eq. (3)). It will be important for models to include the optical impact of CDM to avoid the potential error of misrepresenting light attenuation as models with finer grid resolution are developed, especially in coastal regions.

A similar comparison of the model runs using the "chl&CDM" and the original k_{d} parameterization, Eq. (3), for the entire ocean shows small changes in globally averaged surface and total nutrients, biomass and chlorophyll. Surface nutrients decreased by 3 %, surface biomass decreased by 2 % and surface chlorophyll decreased by 3 %. Total biomass increased by 1 % and total chlorophyll increased by less than 1 % when CDM was included. The differences in attenuation depth between "chl&CDM" and the original k_{d} parameterization are between 0 m to 2 m for large areas of the ocean, as shown in Fig. 16. As mentioned in the Methodology section, the chlorophyll term has a smaller coefficient and exponent in Eq. (5) compared to Eq. (3). Separating the optical contribution of chlorophyll and CDM into two terms gave less weight to the chlorophyll term. In some regions with little attenuation by CDM, there was decreased surface attenuation in the model run that included CDM due to the decreased attenuation by the chlorophyll term. As a result, there are more areas where the difference in attenuation is equal to or greater than 0, which can be seen in a comparison of Fig. 16 and Fig. 9, panel (a). The attenuation depth increased by an average of 0.9 m in locations where the difference in attenuation depth was positive. Based on these results, we find that the biological model error from explicitly excluding the optical impact of CDM by using Eq. (3) to be small for the open ocean. The biological implication for ESMs using Eq. (3) is most profound for coastal regions, as described in the previous paragraph.

4 Conclusions

This paper addressed the impact of colored detrital matter on biological production by altering the attenuation of the in-water light field in the GFDL CM2Mc Earth System Model with BLING biogeochemistry. Light absorption by detrital matter and CDOM, a_{dg}, was prescribed using a satellite dataset with near-complete global surface ocean coverage. Results show that increasing light limitation can decouple surface trends in modeled biomass and macronutrients. Although increased biomass is usually associated with high productivity and decreased nutrients, this was not the case in our light-limited model runs. Surface chlorophyll, biomass and nutrients all increased together. These changes can be attributed to increased biological productivity in the upper water column and decrease below, which increased surface chlorophyll and biomass while simultaneously decreasing depth-integrated biomass. The diminished total biomass left excess nutrients in the water column that were eventually delivered to the surface, elevating surface macronutrient concentrations. While absolute changes in chlorophyll and macronutrient concentrations were small, one key implication of this model experiment is that surface biomass trends may not reflect how light limitation is reducing ecosystem productivity. Understanding changes in ecosystem productivity requires both surface and depth-resolved information.

Adding the optical impact of CDM decreased integrated coastal biomass and chlorophyll concentration by 18 %. Meanwhile, surface chlorophyll concentration in coastal regions increased by 35 %. The open ocean biome analysis showed how, in the BLING model, changes in surface chlorophyll and biomass over the upper 200 m in various biomes depend on a combination of light and nutrient availability. In the high latitudes, adding CDM to the light-only limited Northern Hemisphere vs. the iron-light colimited Southern Hemisphere seemed to have different impacts on biomass decline. In the low- to mid-latitudes, the impact of circulation on light availability for phytoplankton determined the structure of the chlorophyll profile and the response of that biome to a shrinking euphotic zone. These results highlight the biomes that may be most vulnerable to changes in biomass and chlorophyll

if met with changes in light availability. For example high-latitude biomes that were already light limited experienced the greatest drop in biomass from additional light limitation.

In this study, the k_{d} parameterization was developed with measurements from several major regions of the global oceans but did not comprehensively represent the entire ocean's optical properties. The model results showed greatest changes in biomass in the Northern Hemisphere polar and subpolar regions, but our parameterization did not include in situ data from these regions. The spatial distribution of a_{dg} was fixed, so it could not respond to changes in the light field as chlorophyll concentration is able to do in the CM2Mc-BLING coupled physical-biogeochemical model configuration. The a_{dg} values were constant with time so the seasonal cycle was not represented. An analysis of satellite monthly climatology data shows there is more variability near river mouths and equatorial upwelling zones (not shown), indicating these areas would be most affected by including annual cycles. Furthermore, surface values were held constant throughout the water column. Resolving these simplifications may have important impacts. An interactive CDOM tracer would be best suited for such a task, once the mechanisms that control the production and degradation of CDM are better understood. Previous work has elucidated some potential sources and sinks of CDOM to the ocean, including in situ production by heterotrophic microbial activity (Nelson et al., 2004), delivery by freshwater input from terrestrial sources and degradation by photobleaching when exposed to intense light conditions (Blough and DelVecchio, 2002). Recently, Nelson et al. (2010) showed the depth-resolved cross-sections of a_{CDOM} through the major ocean basins approximately follow apparent oxygen utilization contours. This suggests that oxygen might be used to improve modeling depth-dependent CDOM distributions in the future. Dutkiewicz et al. (2015) demonstrate a method for modeling an interactive CDOM tracer as a fraction of dissolved organic material production. Similar to the work presented in our paper, Dutkiewicz et al. (2015) compared model runs with and without the optical impact of CDOM and detrital matter. They found greater productivity and nutrient utilization at higher latitudes when CDOM and detrital matter were omitted, resulting in less nutrient delivery and consequently less biomass in lower latitudes. Their more sophisticated biogeochemical model was also able to evaluate changes in the prevalence of

phytoplankton types associated with changes in the in-water light spectrum from including and removing CDOM and detrital matter. This particular method does not include the key process of terrestrial CDOM delivery. Modeling land sources of CDOM would be of particular importance to regions where CDOM abundance is in flux due to changes in the volume and composition freshwater runoff. In the Arctic Ocean, CDOM is of primary importance in determining the non-water absorption coefficient of light and its relatively concentrated presence increases energy absorbed in the mixed layer by trapping incoming shortwave radiation (Pegau, 2002). Hill (2008) used a radiative transfer model to find the absorption of shortwave radiation by CDOM can increase energy absorbed by the mixed layer by 40 % over pure seawater and this additional energy can account for 48 % of springtime ice melt by water column heating. These impacts should be incorporated into future earth system models and existing higher resolution regional models to more accurately simulate the ocean heat budget and marine biogeochemistry.

Acknowledgements. This work was supported by NASA Headquarters under the NASA Earth and Space Science Fellowship Program – Grant NNX14AK98H. We thank contributors to the NASA SeaBASS data archive which made this work possible. We are grateful for the insightful comments provided by two anonymous reviewers and editor Laurent Bopp.

References

Blough, N. V. and DelVecchio, R.: Chapter 10: Chromophoric DOM in the Coastal Environment, in: Biogeochemistry of Marine Dissolved Organic Matter, edited by: Hansell, D. A., and Carlson, C. A., Academic Press, San Diego, 509–546, doi:10.1016/B978-012323841-2/50012-9, 2002.

Dunne, J. P., Armstrong, R. A., Gnanadesikan, A., and Sarmiento, J. L.: Empirical and mechanistic models for the particle export ratio, Global Biogeochem. Cy., 19, GB4026, doi:10.1029/2004GB002390, 2005.

Dutkiewicz, S., Hickman, A. E., Jahn, O., Gregg, W. W., Mouw, C. B. and Follows, M. J.: Capturing optically important constituents and properties in a marine biogeochemical and ecosystem model, Biogeosciences Discuss., 12, 2607–2695, doi:10.5194/bgd-12-2607-2015, 2015.

Eppley, R.: Temperature and phytoplankton growth in the sea, Fishery Bulletin, 70, 1063–1085, 1972.

Galbraith, E. D., Gnanadesikan, A., Dunne, J. P., and Hiscock, M. R.: Regional impacts of iron-light colimitation in a global biogeochemical model, Biogeosciences, 7, 1043–1064, doi:10.5194/bg-7-1043-2010, 2010.

Galbraith, E. D., Kwon, E. Y., Gnanadesikan, A., Rodgers, K. B., Griffies, S. M., Bianchi, D., Sarmiento, J. L., Dunne, J. P., Simeon, J., Slater, R. D., Wittenberg, A. T., and Held, I. M.: Climate Variability and Radiocarbon in the CM2Mc Earth System Model., J. Climate, 24, 4230–4254, 2011.

Garcia, H. E., Locarnini, R. A., Boyer, T. P., Antonov, J. I., Baranova, O., Zweng, M., Reagan, J., and Johnson, D.: World Ocean Atlas 2013, Volume 4: Dissolved Inorganic Nutrients (phosphate, nitrate, silicate), NOAA Atlas NESDIS 76, edited by: Levitus, S. and Mishonov, A., 2014.

Gnanadesikan, A. and Anderson, W. G.: Ocean water clarity and the ocean general circulation in a coupled climate model., J. Phys. Oceanogr., 39, 314–332, 2009.

Gregg, W. W. and Casey, N. W.: Modeling coccolithophores in the global oceans, Deep Sea Res. Pt. II, 54, 447–477, doi:10.1016/j.dsr2.2006.12.007, 2007.

Hill, V. J.: Impacts of chromophoric dissolved organic material on surface ocean heating in the Chukchi Sea, J. Geophys. Res.-Oceans, 113, C07024, doi:10.1029/2007JC004119, 2008.

Manizza, M., Le Quéré, C., Watson, A. J., and Buitenhuis, E. T.: Bio-optical feedbacks among phytoplankton, upper ocean physics and sea-ice in a global model, Geophys. Res. Lett., 32, L05603, doi:10.1029/2004GL020778, 2005.

Morel, A.: Optical modeling of the upper ocean in relation to its biogenous matter content (case I waters), J. Geophys. Res.-Oceans, 93, 10749–10768, doi:10.1029/JC093iC09p10749, 1988.

Murtugudde, R., Beauchamp, J., McClain, C. R., Lewis, M., and Busalacchi, A. J.: Effects of penetrative radiation on the upper tropical ocean circulation., J. Climate, 15, 470–486, 2002.

Nelson, N. B. and Siegel, D. A.: The global distribution and dynamics of chromophoric dissolved organic matter, Annual Review of Marine Science, 5, 447–476, doi:10.1146/annurev-marine-120710-100751, pMID: 22809178, 2013.

Nelson, N. B., Carlson, C. A., and Steinberg, D. K.: Production of chromophoric dissolved organic matter by Sargasso Sea microbes, Mar. Chem., 89, 273–287, doi:10.1016/j.marchem.2004.02.017, 2004.

Nelson, N. B., Siegel, D. A., Carlson, C. A., and Swan, C. M.: Tracing global biogeochemical cycles and meridional overturning circulation using chromophoric dissolved organic matter, Geophys. Res. Lett., 37, L03610, doi:10.1029/2009GL042325, 2010.

Ohlmann, J. C. and Siegel, D. A.: Ocean radiant heating. Part II: Parameterizing solar radiation transmission through the upper ocean, J. Phys. Oceanogr., 30, 1849–1865, doi:10.1175/1520-0485(2000)030<1849:ORHPIP>2.0.CO;2, 2000.

Pegau, W. S.: Inherent optical properties of the central Arctic surface waters, J. Geophys. Res.-Oceans, 107, SHE 16-1–SHE 16-7, doi:10.1029/2000JC000382, 2002.

Pope, R. M. and Fry, E. S.: Absorption spectrum (380-700nm) of pure water. II. Integrating cavity measurements, Appl. Opt., 36:8710–8723., doi:10.1364/AO.36.008710, 1997.

Reynolds, R. W., Rayner, N. A., Smith, T. M., Stokes, D. C., Wang, W.: An improved in situ and satellite SST analysis for climate, J. Climate, 15:1609–1625., doi:10.1175/1520-0442(2002)015<1609:AIISAS>2.0.CO;2, 2002.

Sarmiento, J. L. and Gruber, N.: Ocean Biogeochemical Dynamics, Princeton University Press, Princeton, New Jersey, 2006.

Sarmiento, J. L., Slater, R., Barber, R., Bopp, L., Doney, S. C., Hirst, A. C., Kleypas, J., Matear, R., Mikolajewicz, U., Monfray, P., Soldatov, V., Spall, S. A., and Stouffer, R.: Response of ocean ecosystems to climate warming, Global Biogeochem. Cy., 18, GB3003, doi:10.1029/2003GB002134, 2004.

Siegel, D. A., Maritorena, S., Nelson, N. B., and Behrenfeld, M. J.: Independence and interdependencies among global ocean color properties: reassessing the bio-optical assumption, J. Geophys. Res.-Oceans, 110, C07011, doi:10.1029/2004JC002527, 2005.

Werdell, P. J. and Bailey, S. W.: An improved in-situ bio-optical data set for ocean color algorithm development and satellite data product validation, Remote Sens. Environ., 98, 122–140, doi:10.1016/j.rse.2005.07.001, 2005.

Yoder, J. A. and Kennelly, M. A.: Seasonal and ENSO variability in global ocean phytoplankton chlorophyll derived from 4 years of SeaWiFS measurements, Global Biogeochem. Cy., 17, 23-1–23-14, doi:10.1029/2002GB001942, 2003.

Table 1. Surface area by biome, in km^2 with percentage change in area between the two model runs (chl&CDM minus chl-only).

Biome	chl&CDM	% age of total	chl-only	% age of total	% change
Equatorial Upwell	1.86×10^7	6 %	1.86×10^7	6 %	0 %
Equatorial Downwell	8.34×10^6	3 %	8.07×10^6	3 %	3 %
Low Latitude Upwell	6.32×10^7	21 %	6.32×10^7	21 %	0 %
Permanently Stratified	1.01×10^8	34 %	9.89×10^7	33 %	2 %
Seasonally Stratified	3.93×10^7	13 %	4.11×10^7	14 %	−4 %
Subpolar NH	1.22×10^7	4 %	1.35×10^7	4 %	−9 %
Ice NH	1.17×10^7	4 %	9.81×10^6	3 %	19 %
Subpolar SH	2.33×10^7	8 %	2.43×10^7	8 %	−4 %
Ice SH	2.37×10^7	8 %	2.27×10^7	8 %	4 %

Table 2. Difference in surface chlorophyll $\mathrm{mg\,m^{-3}}$, biomass $\mathrm{mg\,C\,m^{-3}}$ and macronutrient μM concentrations, chl&CDM minus chl-only. Surface values are the average over the top 10 m. All surface changes are statistically significant to three standard deviations. Statistical significance tests were performed on decadally smoothed data from the the final 100 years of the two model runs.

Biome	Δ chl	% Δ	Δ biomass	% Δ	Δ nutrient	% Δ
Equatorial Upwell	0.28	22 %	4.5	16 %	0.053	14 %
Equatorial Downwell	0.23	24 %	4.2	17 %	0.052	24 %
Low Latitude Upwell	0.21	21 %	3.1	15 %	0.038	20 %
Permanently Stratified	0.18	15 %	2.0	10 %	0.036	13 %
Seasonally Stratified	0.52	7 %	2.2	5 %	0.066	15 %
Subpolar NH	0.83	9 %	4.2	7 %	0.071	19 %
Ice NH	0.90	18 %	7.7	14 %	0.10	23 %
Subpolar SH	0.29	7 %	0.97	3 %	0.041	3 %
Ice SH	0.18	11 %	1.3	6 %	0.038	2 %

Table 3. Difference in chlorophyll $\mathrm{mg\,m^{-2}}$, biomass $\mathrm{mg\,C\,m^{-2}}$ and macronutrients $\mathrm{mmol\,m^{-2}}$ between the two model runs (chl&CDM minus chl-only), integrated over the upper 200 m.

Biome	Δ chl	% Δ	Δ biomass	% Δ	Δ nutrient	% Δ
Equatorial Upwell	−1.7	−7 %	−87	−6 %	15	8 %
Equatorial Downwell	−1.2	−5 %	−67	−5 %	17	11 %
Low Latitude Upwell	−0.74	−4 %	−38	−3 %	13	9 %
Permanently Stratified	−0.77	−4 %	−61	−4 %	11	11 %
Seasonally Stratified	−2.2	−5 %	−127	−5 %	16	13 %
Subpolar NH	−8.8	−14 %	−482	−15 %	15	11 %
Ice NH	−2.2	−5 %	−179	−8 %	22	16 %
Subpolar SH	−1.6	−5 %	−139	−6 %	7.4	2 %
Ice SH	−2.1	−9 %	−165	−10 %	5.3	1 %

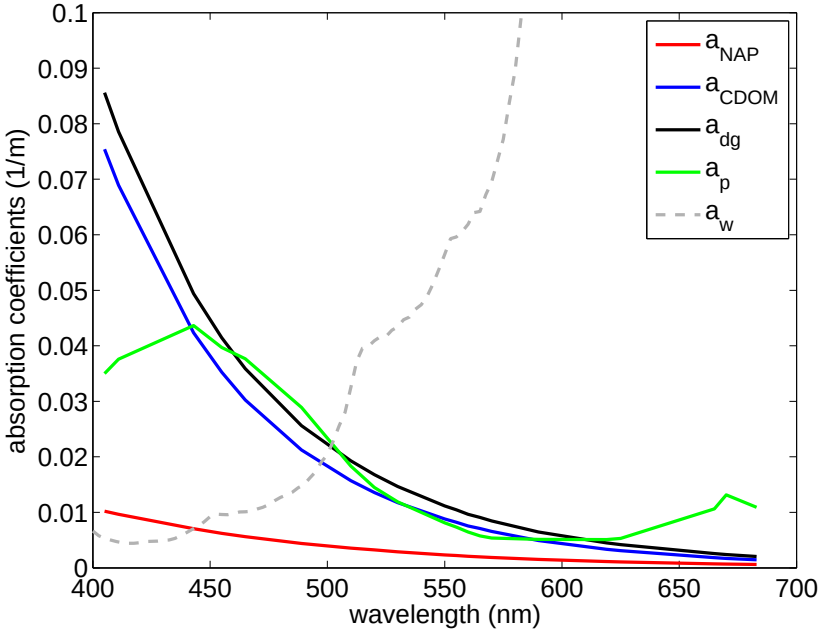

Figure 1. Median IOP spectra from NOMAD dataset and absorption spectrum of pure water in gray. In the visible spectrum, CDOM absorption is strongest in the blue and decreases exponentially with increasing wavelength. The absorption spectrum of pure water is 0.0434 m^{-1} at 530nm and increases to 0.6 m^{-1} at 700nm, exceeding the axis limits shown here. (Pope and Fry, 1997) The absorption spectrum of particles (including phytoplankton), a_p, absorbs strongly in the red wavelengths compared to NAP and CDOM.

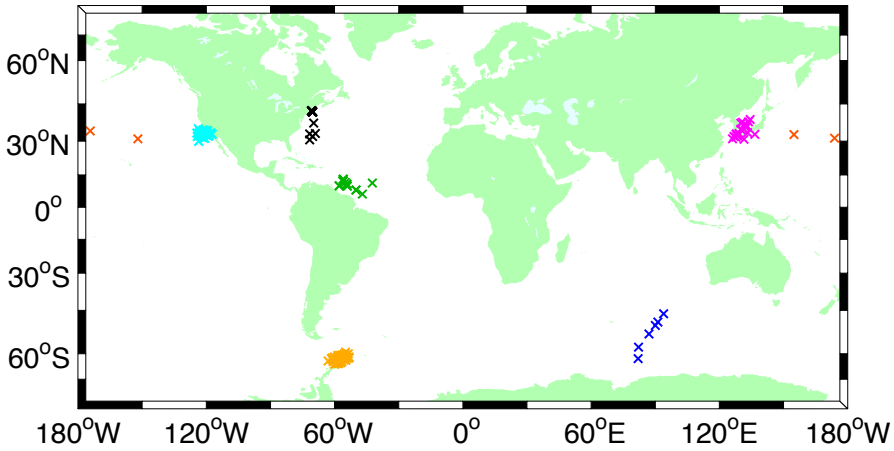

Figure 2. Map of stations with locations of the 244 in-situ measurements used to develop the $k_{\mathrm{d}}(\mathrm{bg})$ parameterization with CDM, Eq. (5), color coded by arbitrarily grouped by region: (1) western Atlantic, northern cluster in black; (2) western Atlantic, Amazon river outflow and offshore stations in green; (3) Antarctic peninsula in orange; (4) Southern Ocean in blue; (5) western Pacific in magenta; (6) stations across the Pacific ocean in red and (7) eastern Pacific in cyan.

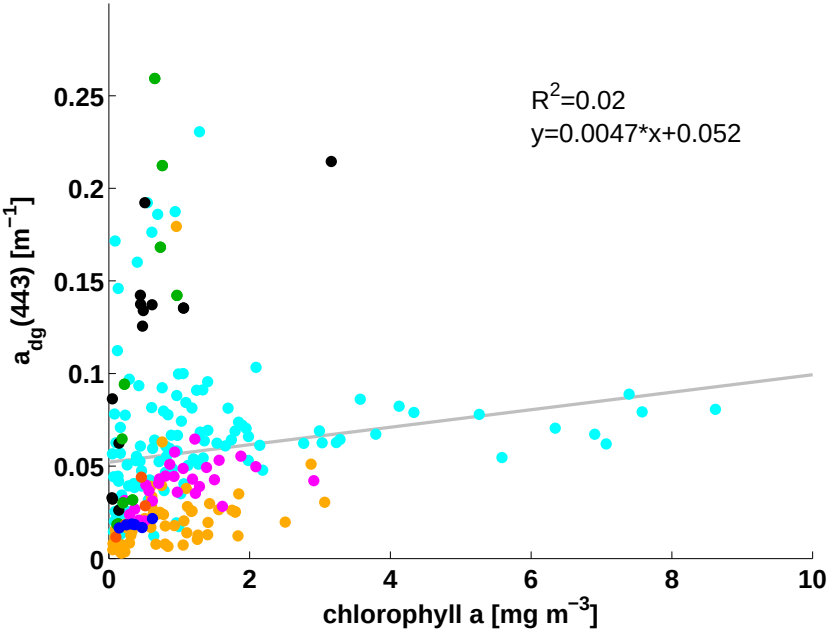

Figure 3. Scatterplot of 244 in-situ chlorophyll-a concentration and $a_{dg}(443)$ concurrent measurements from the NOMAD dataset used to develop the $k_{\mathrm{d}}(\mathrm{bg})$ parameterization with CDM, Eq. (5). Color coding corresponds to regional groupings from Fig. 2.

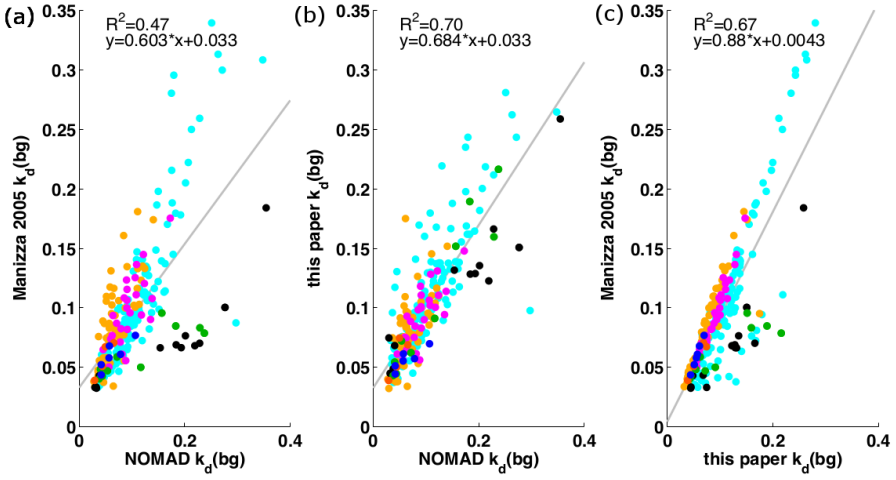

Figure 4. (a) and **(b)** Scatterplots comparing observed $k_{\mathrm{d}}(\mathrm{bg})$ from the NOMAD dataset and modeled $k_{\mathrm{d}}(\mathrm{bg})$ using two different parameterizations, Eqs. (3) and (5). The modeled $k_{\mathrm{d}}(\mathrm{bg})$ values are calculated from in situ chlorophyll-a and $a_{\mathrm{dg}}(443)$ measurements corresponding to the observed $k_{\mathrm{d}}(\mathrm{bg})$ values on the x-axis. **(c)** Comparison of Eqs. (3) and (5) applied to NOMAD in situ chlorophyll concentration and $a_{\mathrm{dg}}(443)$ measurements to calculate $k_{\mathrm{d}}(\mathrm{bg})$. The 0.88 slope on the regression line indicates that when CDM is included, $k_{\mathrm{d}}(\mathrm{bg})$ increases more rapidly than when it depends on chlorophyll concentration alone. Color coding corresponds to regional groupings from Fig. 2.

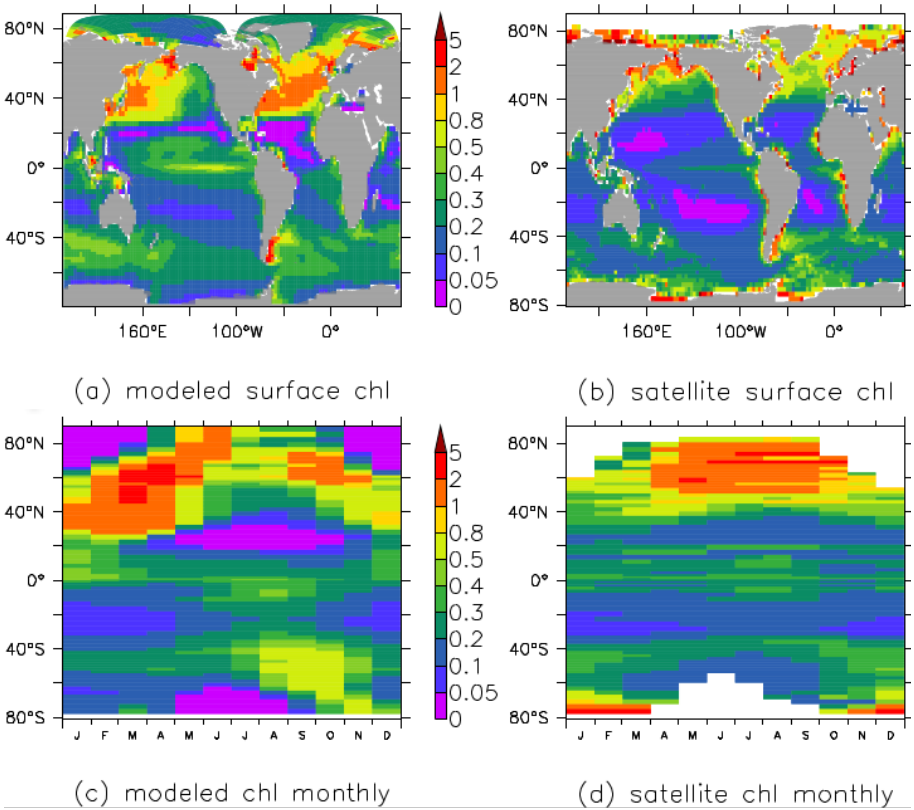

Figure 5. Comparison of **(b, d)** chlorophyll concentration in mg m^{-3} from SeaWiFS satellite observation (Yoder and Kennelly, 2003) used in earlier similar studies and **(a, c)** modeled using GFDL ESM CM2Mc with BLING biogeochemistry. Data shown are from the chl&CDM model run described in Sect. 4 of this paper. Annual average surface distributions are shown in **(a, b)** and monthly average surface concentration by latitude are shown in **(c, d)**.

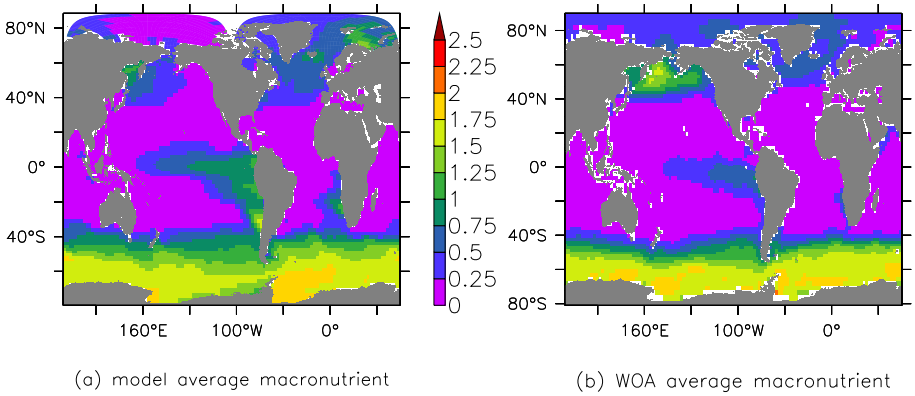

Figure 6. Comparison of **(a)** modeled using GFDL CM2Mc with BLING biogeochemistry and **(b)** measured macronutrient concentration, $\frac{1}{2}(PO_4 + \frac{NO_3}{16})$, from World Ocean Atlas 2013 nitrate and phosphate datasets (Garcia et al., 2014). Concentration in µM.

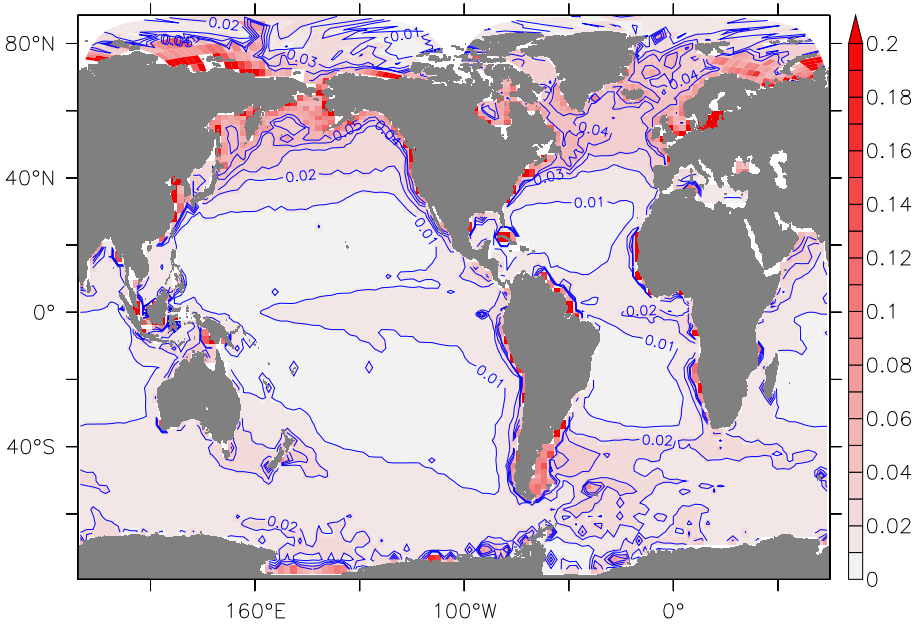

Figure 7. The spatial distribution of $a_{\mathrm{dg}}(443)$ as prescribed in the model runs for this paper, mapped onto the CM2Mc ESM tracer grid with data extrapolated into polar regions.

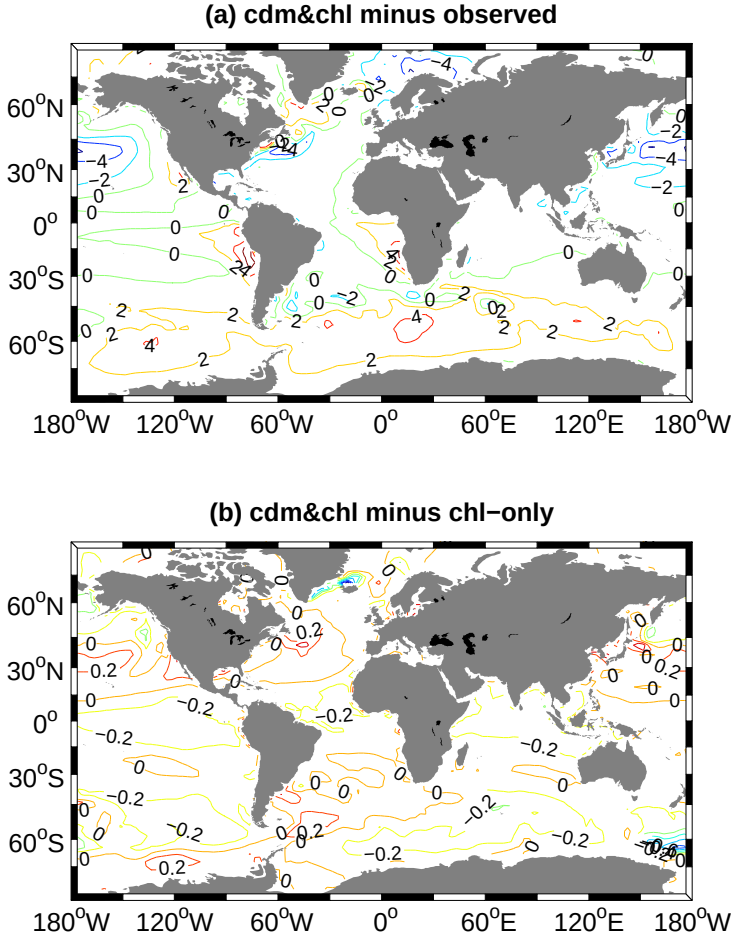
(a) cdm&chl minus observed
60°N
30°N
0°
30°S
60°S
180°W
120°W
60°W
0°
60°E
120°E
180°W
(b) cdm&chl minus chl−only
60°N
30°N
0°
30°S
60°S
180°W
120°W
60°W
0°
60°E
120°E
180°W

Figure 8. Difference in annual average SST in °C for (a) chl&CDM minus observed using the NOAA_OI_SST_V2 dataset (Reynolds, 2002) and (b) chl&CDM minus chl-only.

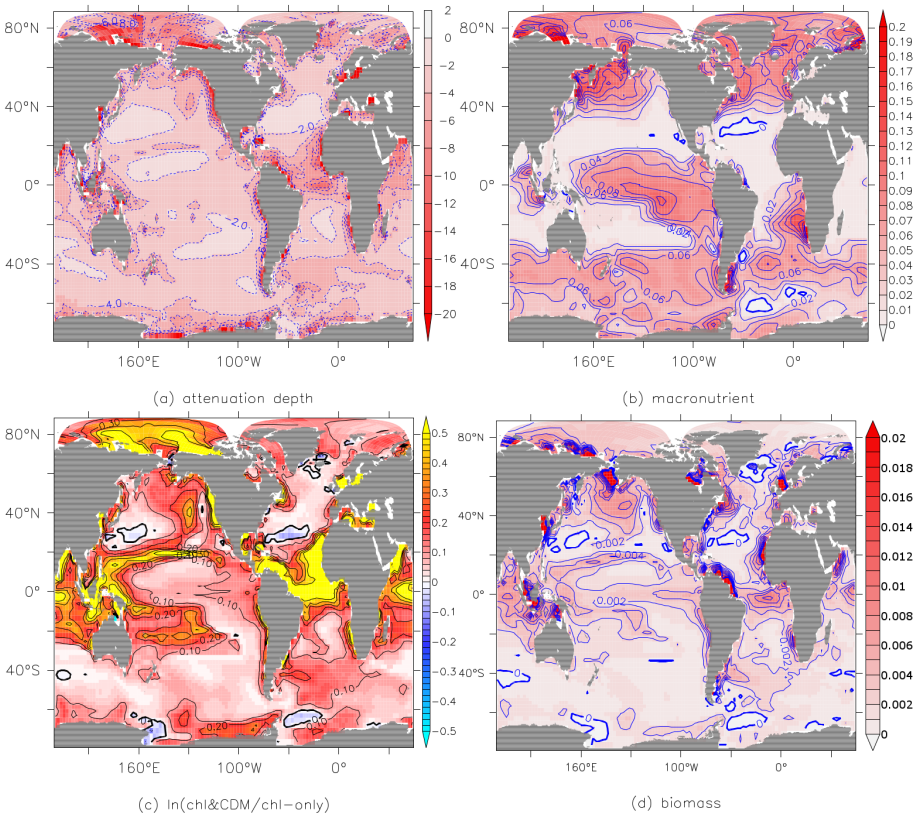

Figure 9. Difference **(a)** attenuation depth m, **(b)** surface macronutrient concentration µM, **(c)** surface chlorophyll concentration and **(d)** surface biomass concentration g C m^{-3}; chl&CDM minus chl-only. Surface values represent the average over the top 10 m. Panel **(c)** shows natural log ratio of chlorophyll concentration from the chl&CDM run over chl-only run, so positive values indicate an increase in chlorophyll in the chl&CDM run.

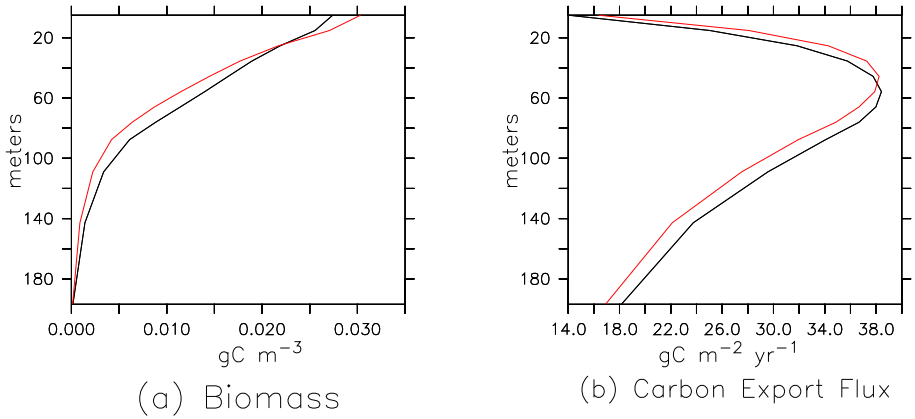

Figure 10. Globally averaged profile of **(a)** biomass in $\mathrm{g\,C\,m^{-3}}$ and **(b)** carbon export flux in $\mathrm{g\,C\,m^{-2}\,yr^{-1}}$. Black line shows data from the chl-only run, red line represents chl&CDM run.

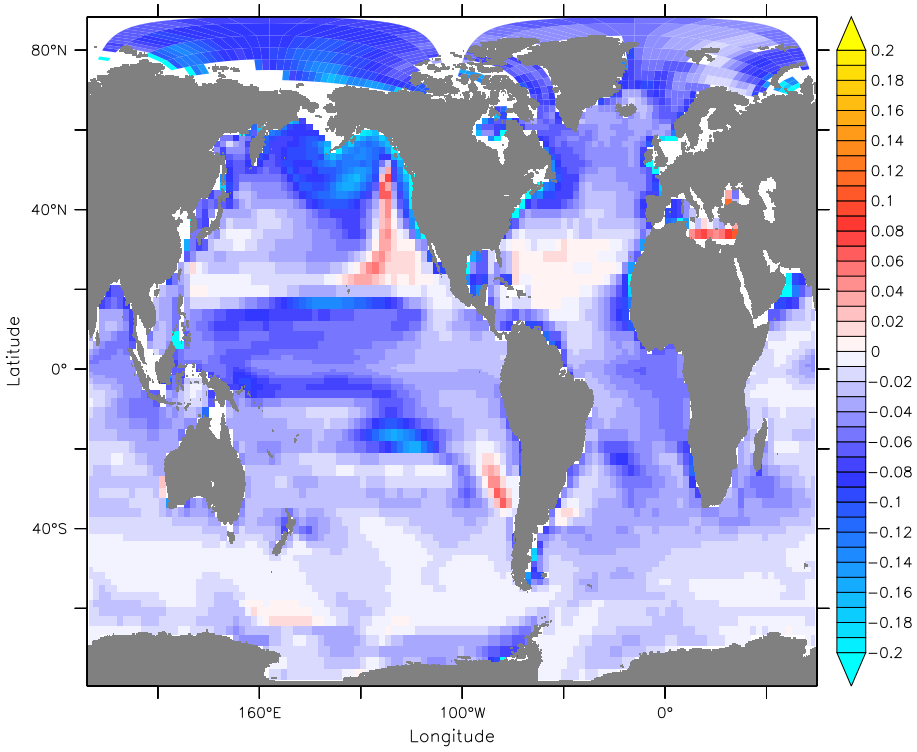

Figure 11. Difference in E_{bp}, chl&CDM model run minus chl-only model run.

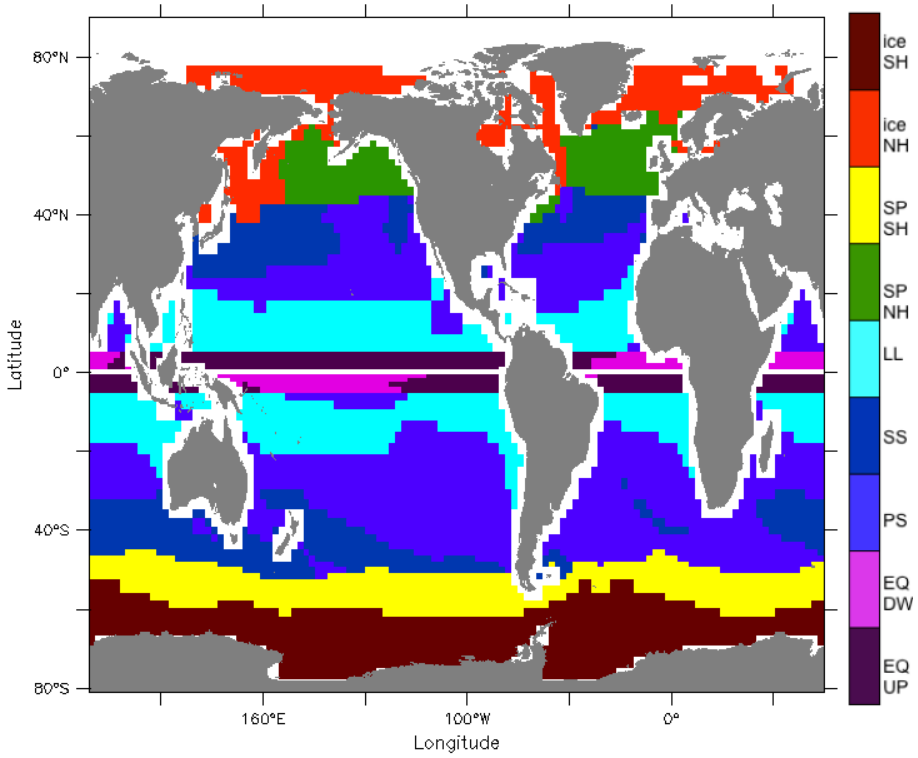

Figure 12. Biomes as defined by Sarmiento et al. (2004) applied to GFDL CM2Mc with chl&CDM k_{d} parameterization, Eq. (5). Legend abbreviations: ice = marginal ice zone, SP = subpolar, LL = lower latitude, SS = seasonally stratified, PS = permanently stratified, EQ DW = equatorial downwelling, EQ UP = equatorial upwelling. Suffixes NH and SH stand for northern hemisphere and southern hemisphere.

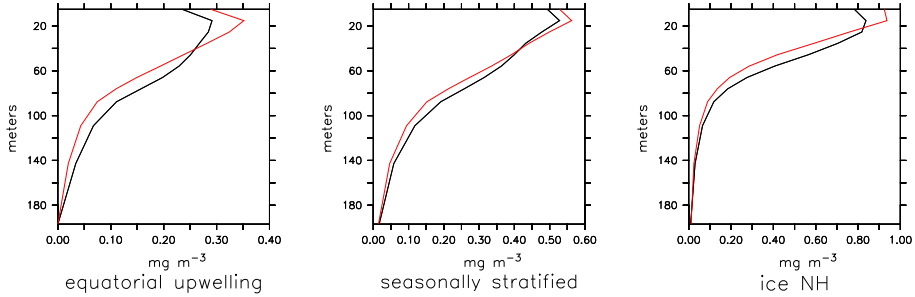

Figure 13. The depth profile of chlorophyll concentration $\mathrm{mg\,m^{-3}}$ in three biomes. The black line indicates the chl-only run, red line represents chl&CDM run. The equatorial upwelling and seasonally stratified biomes show increased peaks in the deep chlorophyll maximum (DCM) when CDM is included. All three biomes show increased chlorophyll near the surface, but diminished chlorophyll at depth.

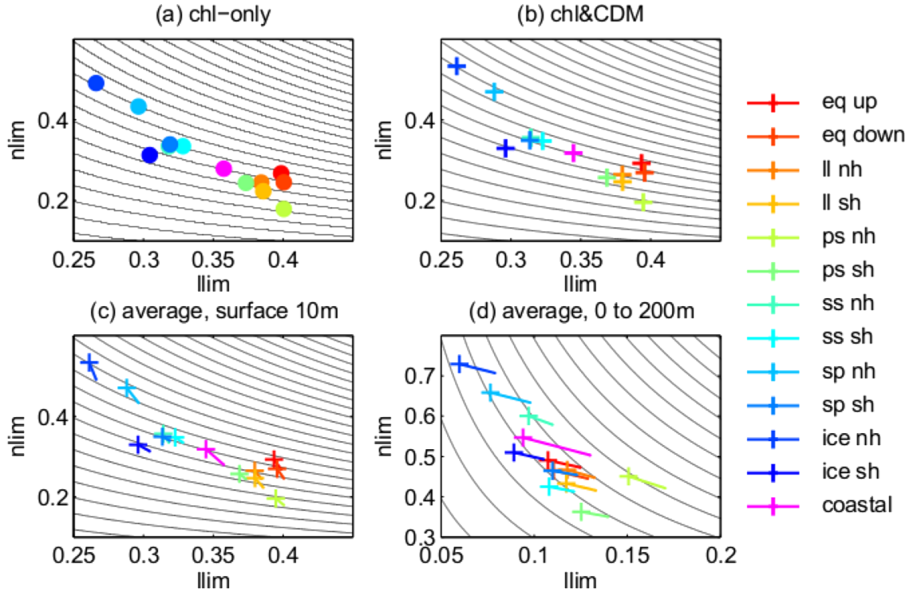

Figure 14. Light and nutrient limitation scaling factors for open ocean biomes and coastal regions. **(a)** Average nlim, llim for chl-only model run, from 0 to 10 m **(b)** average nlim, llim for chl&CDM model run, from 0 to 10 m **(c)** vectors connecting coordinates from panel **(a, b)**, average from 0 to 10 m. **(d)** Vectors starting at coordinates from chl-only model run and terminating with an "x" at values from chl&CDM model run, average from 0 to 200 m. Legend abbreviations: ice = marginal ice zone, sp = subpolar, ss = seasonally stratified, ps = permanently stratified, ll = lower latitude, eq up = equatorial upwelling, eq down = equatorial downwelling, coastal = coastal regions, defined as the grid cells adjacent to land. Suffixes nh and sh stand for Northern Hemisphere and Southern Hemisphere.

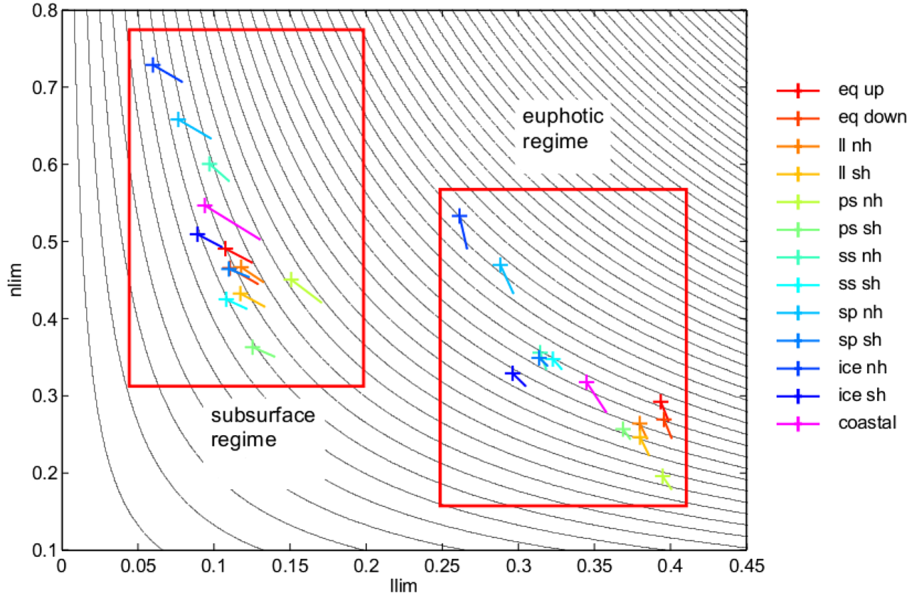

Figure 15. All vectors from Fig. 14c and d, on the same plot. Vectors for nlim, llim values averaged over the upper 10 m occupy the "euphotic regime" and values averaged over the upper 200 m occupy the "subsurface regime".

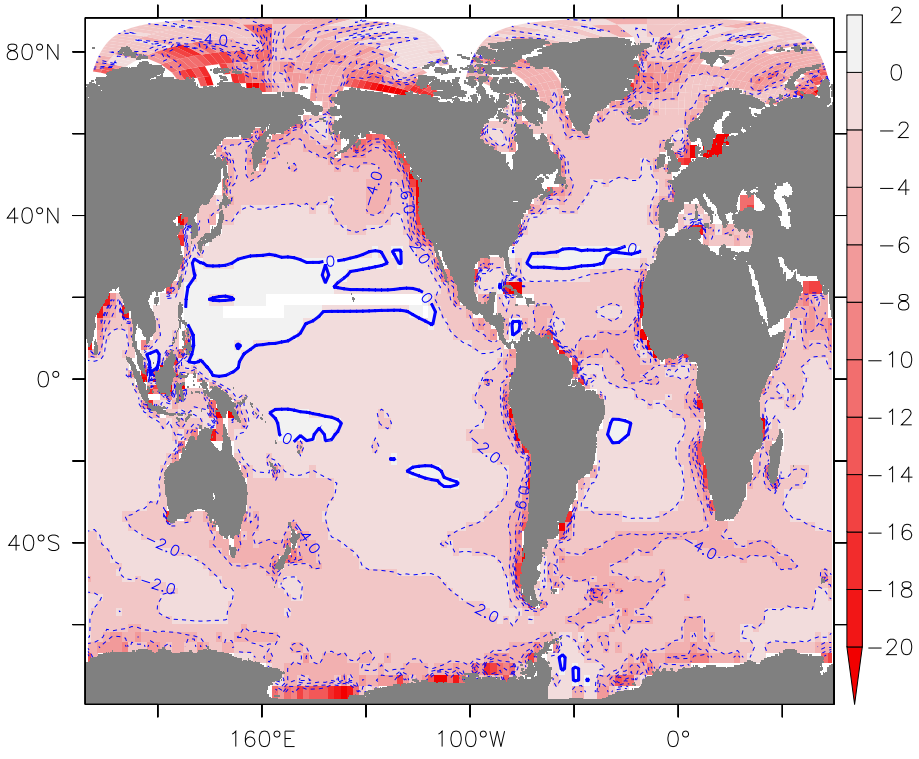

Figure 16. Difference in attenuation depth in m; chl&CDM minus model run using Eq. (3).